A Secondary-Side Semiactive 3-Phase Interleaved Resonant Converter Employing Multimode Modulation Scheme for Fast EV Charger Applications

Zhe Shi, Yu Tang, *Senior Member, IEEE*, Yuliang Zhang, Yingjun Guo, Hexu Sun, *Senior Member, IEEE*, and Lin Jiang, *Member, IEEE*

***Abstract*—A secondary-side semiactive three-phase interleaved (SS-SA3PI) resonant converter employing a multimode modulation scheme for fast EV charger applications is proposed. A multimode modulation scheme is used to widen the output voltage range without dynamic switching problems. By using secondary-side semiactive control, the resonant converter does not need to operate in the $f_s < f_r$ state to achieve boost operation. The minimum switching frequency of the converter is equal to the resonant frequency, which reduces the size of the magnetic components. Thus, the power density of the converter is improved. Compared with the traditional 3-phase interleaved *LLC* converter controlled by PFM, this converter widens the output voltage range without adding any circuit components. This article introduces the control mode, working principle and characteristics of the proposed converter in detail. A 10 kW experimental prototype is built to realize the output voltage of 100–1000V, which verifies the feasibility and effectiveness of the scheme.**

***Index Terms*—Fast electric vehicle (EV) charger, multimode modulation scheme, power density, secondary-side semiactive three-phase interleaved (SS-SA3PI) resonant converter, wide output voltage range.**

Manuscript received 4 January 2022; revised 7 April 2022; accepted 30 May 2022. Date of publication 3 June 2022; date of current version 26 July 2022. This work was supported in part by the Hebei Province Science Fund for Distinguished Young Scholars under Grant E2020202140, in part by the National Natural Science Foundation of China under Grants 51677084 and 52130710, in part by the Support Program (III) for 100 Outstanding Innovative Talents in Universities of Hebei Province under Grant SLRC2019025, and in part by the Hebei Provincial Central Government Guided Local Science and Technology Development Fund Project under Grant 216Z4401G. Recommended for publication by Associate Editor A. Barrado. *(Corresponding author: Yu Tang.)*

Zhe Shi and Yu Tang are with the State Key Laboratory of Reliability and Intelligence of Electrical Equipment, Hebei University of Technology, Tianjin 300130, China, and also with the Hebei Key Laboratory of Electromagnetic Field and Electrical Apparatus Reliability, Hebei University of Technology, Tianjin 300401, China (e-mail: 202011401002@stu.hebut.edu.cn; 202021401072@stu.hebut.edu.cn).

Yuliang Zhang is with the Shijiazhuang Tonghe Electronic Technology Co., Ltd, Shijiazhuang 050000, China (e-mail: zhangyuliang@sjzthdz.com).

Yingjun Guo and Hexu Sun are with the Hebei University of Science and Technology, Shijiazhuang 050018, China (e-mail: 202011401001@mail.stu.hebut.edu.cn; 202031404079@stu.hebut.edu.cn).

Lin Jiang is with the Department of Electrical Engineering and Electronics, University of Liverpool, L69 3BX Liverpool, U.K. (e-mail: l.jiang@liverpool.ac.uk).

Color versions of one or more figures in this article are available at https://doi.org/10.1109/TPEL.2022.3179974.

Digital Object Identifier 10.1109/TPEL.2022.3179974

I. Introduction

USING electric vehicles (EV) to replace fuel vehicles is one of the effective ways to solve the problem of environmental pollution and greenhouse effect. However, an embarrassing thing about the popularity of EVs is that the charging speed of EVs is slower than the refueling speed of fuel vehicles. For the popularity of EVs, it is necessary to increase the charging power of the charger. The dc/dc part of the charger has become one of the key factors in determining the development of EV [1], [2].

Due to the large output power of the dc/dc PART, some topologies that can achieve zero voltage switching (ZVS), such as *LLC* and phase-shifted full-bridge are widely used. Among these topologies, the ability of *LLC* to achieve soft switching for higher efficiency over the full load range has received a lot of attention [3]–[7].

The current industrial 20 kW constant power charger has become mainstream, and its common dc/dc topology is a three-level *LLC* input series output series/parallel (ISOS/P) structure using Si Mos [8]–[12]. The advantages of changing the rectifier side series or parallel structure through relays are as follows:

1) Wide output voltage range and constant power output voltage range.
2) Low voltage and current stress of rectifier diodes.
3) Low hardware costs.

However, the implementation of three-level *LLC* ISOS/P structure ZVS requires the switching tube body diode to continue the current. The poor Si Mos body diode will cause reverse recovery when the converter is lightly loaded, and the large *di/dt* will cause EMI problems, making the converter face stability and efficiency challenges. Besides, the complex structure and huge amount of circuit components make the layout of the three-level *LLC* ISOS/P converter tight within a limited range, which exacerbates the difficulty of designing the internal air ducts, heat dissipation and circuitry of the charger. Even, it will affect the overall working stability of the converter.

With the application of the third generation semiconductor device SiC in 5G communication, artificial intelligence and EVs, its cost is gradually reducing. SiC power devices have a smaller reverse recovery charge and are suitable for converters where body diodes require current continuation. And the high

operating junction and breakdown field strength of SiC tubes means lower through-state losses and higher conversion efficiency. The current common 20 kW EV charger (250–750V output) using SiC devices is a full-bridge parallel-tube *LLC* structure [13]. When the power of this structure needs to be designed larger, SiC devices with lower internal resistance need to be used, which means higher hardware costs. For this, the three-phase interleaved *LLC* structure provides a solution. Compared with the full-bridge *LLC* structure, its advantages are as follows.

1) Current stress is 2/3 of full-bridge structure.
2) Transformer is Y-connected, automatic current equalization between phases.
3) Same conversion efficiency as full-bridge structure in 30 kW.
4) Low hardware costs.

However, limited control methods limit the voltage regulation capability of the three-phase interleaved *LLC* structure. Refer to the classification and discussion of the full-bridge *LLC* modulation strategy in part [14]. Some modulation strategies that can be extended to the three-phase interleaved *LLC* structure are discussed, although these extended applications may not be published. We divide the modulation strategies that can be applied into three categories.

1) Primary-side inverter network modulation.
2) Resonant network modulation.
3) Secondary side rectification network modulation.

For primary-side inverter network modulation, the output voltage is regulated by adjusting the fundamental harmonic of the resonant network input voltage. There exist two freedoms to adjust the fundamental harmonic of resonant tank input voltage: magnitude and frequency. The use of pulse frequency modulation (PFM) is the most common control method for a three-phase interleaved resonant converter [15]. However, PFM control is considered to be a major drawback of resonant converters [16]. Typically, when a three-phase interleaved resonant converter using SiC devices has a wide output voltage range, the range of switching frequencies will also be wide, which will result in large magnetic component size and core losses. Besides, the inappropriate design will reduce the ZVS range and bring EMI problems. For magnitude modulation, common approaches are pulsewidth modulation (PWM) [17], primary side phase shift modulation (PSPSM) [18], asymmetric PWM [19], and variable input voltage control [20]. However, PWM type of control will lead to complex drive design, current and thermal imbalance. And PSPSM control cannot be extended to the three-phase interleaved resonant converter because the phase angle of each phase is fixed at 120°. The literature [21] extends the method in the literature [17] to a three-phase interleaved structure, which makes the output voltage range of the converter wider. Although PFM control is used, the addition of an additional switching device and its corresponding heat sink cannot be avoided. For variable input voltage control, [22] is similar to the approach implemented in [20], which is particularly suitable for applications with two-stage structure, such as EV chargers, since the output voltage of the PFC is adjustable. This will bring us a positive meaning.

For resonant network modulation, the main control degrees of freedom are: resonant frequency and transformer turn ratio. The main modulation methods based on changing the resonant frequency are: variable inductor control [23], variable capacitor control [24], switched-control capacitor [25] and switched capacitor circuit [26]. There are switching tubes or relays that are commonly used in industry to change the transformer turn ratio. Although all of these modulation strategies can greatly widen the regulation range of the output voltage, they do not avoid additional detection, resonance and switching components. Moreover, switching-type modulation will bring dynamic stability problems.

For secondary side rectification network modulation, two modulation strategies can widen the output voltage range, one is the secondary side PWM (SSPWM) [26], and another one is the secondary side PSM (SSPSM) [27], [28]. In [26], an auxiliary switch is added on the secondary side. The use of PWM control for the auxiliary switches allows the converter to switch from the *LLC* structure to the voltage doubling rectifier structure. Therefore, the voltage gain can be adjusted from 1 to 2. However, SSPWM still adds an extra switch and the heat sink corresponding to this switch, reducing the power density of the converter. A control method of SSPSM is discussed in [27] and [28], which replaces the two lower diodes on the secondary side with two switches. By using SSPSM control, the converter obtains the boost effect. This modulation strategy adds no additional power components, allowing the converter to maintain a high power density and conversion efficiency. However, if applied to ultrawide output voltage applications, a single control method will lose some ZVS range and create EMI problems. A time-delay control (TDC) similar to SSPSM is discussed in [29]–[32], which incorporates PSPFM control to further widen the output voltage regulation range. However, unlike SSPSM, TDC boosts require additional phase detection chips to achieve synchronous rectification. This undoubtedly poses potential stability problems. Moreover, the implementation of boost operation above the resonance point broadens the ZVS range of the converter but also results in a loss of voltage gain. All in all, SSPSM is a very potential regulatory strategy.

To meet the future requirements of higher power for EV chargers while achieving a wide output voltage range without reducing the power density of the converter, this article proposes a SS-SA3PI resonant converter employing a multimode modulation scheme to solve the above problems. The main contributions of this article are as follows.

1) The minimum switching frequency of the proposed SS-SA3PI resonant converter is the resonant frequency, which facilitates the reduction of the size of the magnetic components and thus increases the power density of the converter.
2) The employed multimode modulation scheme can enlarge the output voltage range to the greatest extent.
3) The converter also realizes a full range of soft switching, which is beneficial to reducing EMI and improving conversion efficiency. In addition, this article also simplifies the formula derivation under the boost mode, making the control method easy to implement in an online controller.

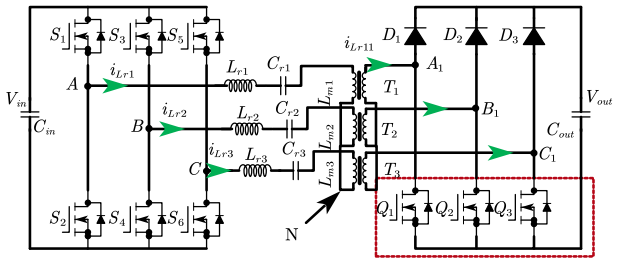

Fig. 1. Proposed SS-SA3PI resonant converter.

II. Proposed Converter and Working Principle

The proposed SS-SA3PI resonant converter is shown in Fig. 1. A three-phase bridge high-frequency inverter network consisting of six SiC Mos S_1–S_6 on the primary side of the transformer. Three SiC Mos Q_1–Q_3 and three diodes D_1–D_3 form a three-phase semiactive bridge rectification network on the secondary side of the transformer. Two three-phase bridge networks are connected by three identical sets of high-frequency transformers T and a three-phase staggered resonant network composed of L_r, C_r. The transformers are connected in a Y-shape to balance the currents between the bridge arms of each phase.

In the EV charger applications, it is generally a two-stage structure, and the output dc-bus voltage of ac/dc converter is 660–850 V at PF = 1. Considering the actual application background of the proposed converter, the converter needs to output 100–1000 V at the input voltage V_{in} is 660–850 V to match different EV battery pack voltages. According to the < Qualification capability verification standard for EV charging equipment suppliers >, the converter is required to BE capable of constant maximum power output at an output voltage of 400–750 V. Thus, the maximum output current of the proposed converter is limited to 25 A. Depending on the different controlled quantities of the converter, we divide the used multimode modulation scheme into three modes: boost mode (secondary-side semiactive control); variable bus voltage control mode; and buck mode.

A. Working Principle of Boost Mode

The typical operating waveform of SS-SA3PI resonant converter under secondary-side semiactive control is shown in Fig. 2. The switching frequency f_s is equal to the resonant frequency f_r. Switching tubes S_1–S_6, the upper and lower switching tubes of each bridge arm are on complementarily, and the duty cycle is fixed at 0.5. The bridge arms of each phase are staggered by 120° in one period. The basic principle of secondary-side semiactive control in boost mode is that: when S_1, S_4, and S_5 are on, the transformer secondary Q_1 is on and the secondary current flows positively through Q_1 and the parasitic diode along Q_2 short-circuits the transformer T_1, T_2 secondary winding. At this time, the input voltage V_{in} charges to the resonant network. When Q_1 is turned OFF, the secondary side of the converter continues to rectify the current. During rectification, the input voltage and the resonant network discharge together to the load to obtain a boost effect. The same is true for S_3, S_6, S_1conduction and S_5, S_2, S_3 conduction. We name the time when S_1, S_4, S_5

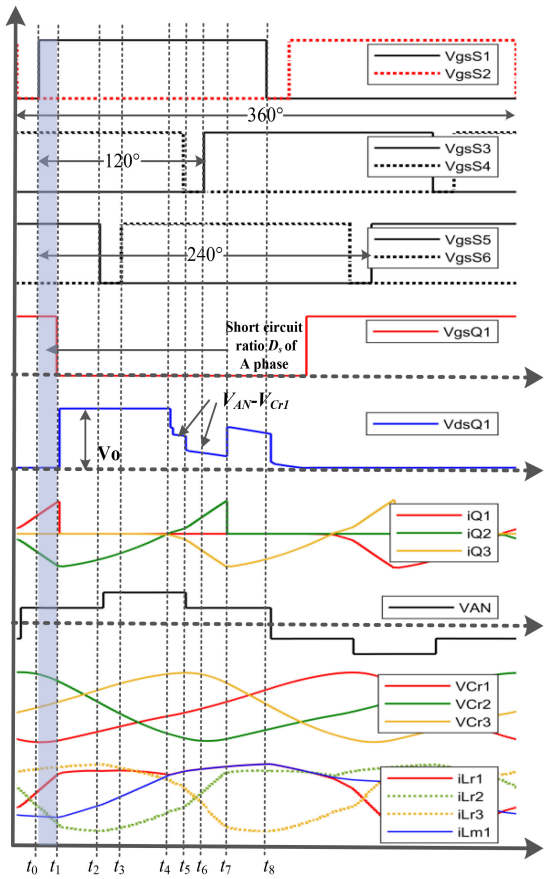

Fig. 2. Boost mode waveform under secondary-side semiactive control.

and Q_1 pulses overlap as the secondary side duty cycle D_s. The adjustment of the D_s can be achieved by adjusting the hysteresis phase of $Q_{1\text{-}3}$ with respect to $S_{2\text{-}6}$. The larger of the D_s, the larger the resonant network energy storage and the higher the boost ratio. In this mode, the bus voltage is fixed at 850 V, when the output voltage is 850–1000 V, the converter relies on adjusting the D_s to achieve the voltage gain change. For easy understanding, we divided the converter into eight modes in half a cycle and drew the equivalent circuit diagram, as shown in Fig. 3.

1) *Mode a (t_0–t_1):* At the moment of t_0, S_1, S_2 commutation ends, A-phase bridge arm resonant current i_{Lr1} is negative, S_1 turn-ON signal V_{gss1} arrives, S_1 realizes ZVS-ON. At this time, transformer primary switching tubes S_1, S_4, S_5 conduct, secondary Q_1 conducts, secondary current flows positively through Q_1, flows through Q_2 parasitic diode to short circuit transformer T_1, T_2 secondary windings. V_{in} charges the resonant network, and the resonant currents i_{Lr1}, i_{Lr2}, and i_{Lr3} increase linearly. At this time, the resonant network structure is A, C phase in parallel with B phase in series. According to the circuit KVL theorem, the resonant current expression can be obtained as

$$i_{Lr1}(t) = i_{Lr1}(t_0)\cos[\omega_r(t-t_0)] + \frac{V_{\text{in}} - u_{Cr}(t_0)}{Z_r}\sin[\omega_r(t-t_0)] \quad (1)$$

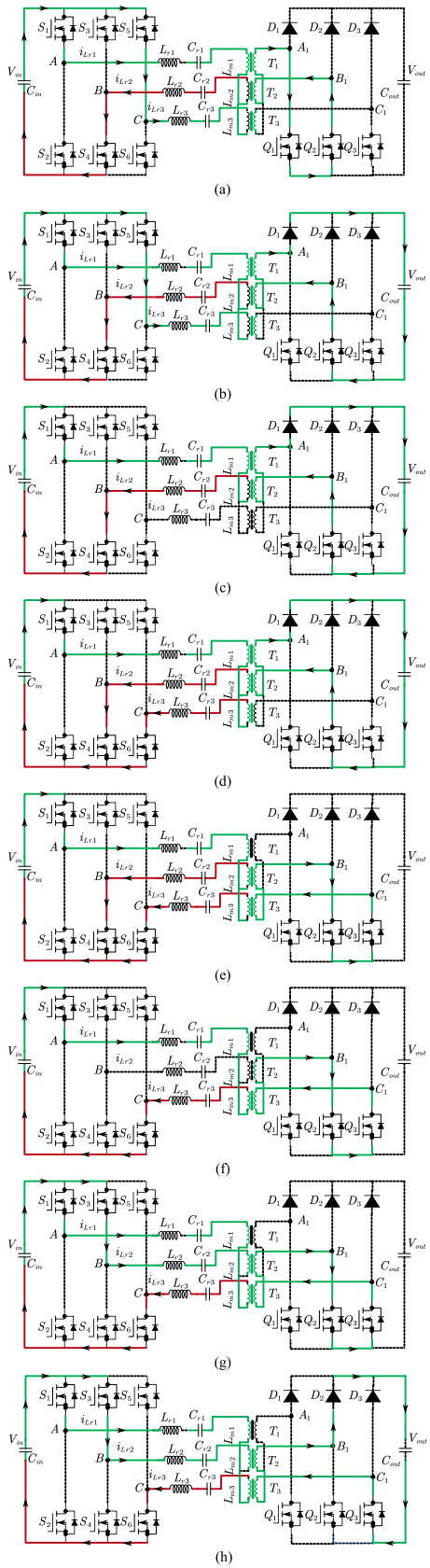

Fig. 3. Equivalent circuit of (a)–(h). (a) Mode a. (b) Mode b. (c) Mode c. (d) Mode d. (e) Mode e. (f) Mode f. (g) Mode g. (h) Mode h.

where the resonant angular frequency is $\omega_r = 1/(L_r/C_r)^{\wedge 2}$, and the characteristic impedance is $Z_r = (L_r/C_r)^{\wedge 0.5}$.

2) *Mode b (t_1–t_2):* Q_1 is turned OFF at t_1, and the secondary windings of transformers T_1 and T_2 are no longer short-circuited, and the secondary current flows through D_1 and Q_2 parasitic diodes for rectification. The primary switching tube action and resonant network structure is the same as the previous mode, at this time, V_{in} and resonant network together discharge to the load. This mode within the resonant network occurs in series resonance, resonant frequency f_r is (2). Where + represents the series connection, the inductor series inductance value is added, the capacitor series capacitance value is the inverse of the capacitance value is added. Similarly, the expression for the resonant current is (3)

$$f_r = \frac{1}{2\pi\sqrt{(L_{r1}//L_{r3} + L_{r2}) \times (C_{r1}//C_{r3} + C_{r2})}} = \frac{1}{2\pi\sqrt{L_r \times C_r}}. \tag{2}$$

3) *Mode c (t_2–t_3):* At the moment of t_2, the switching tubes S_5, S_6 commutate the current. During the dead time, the C-phase bridge arm resonant current i_{Lr3} is positive, i_{Lr3} charges and discharges the S_5, S_6 parasitic capacitors, and i_{Lr3} flows through the S_6 parasitic diode to continue the current. The secondary side of the transformer is the same as the previous mode

$$i_{Lr1}(t) = i_{Lr1}(t_1)\cos[\omega_r(t - t_1)] + \frac{V_{in} - u_{Cr}(t_1) - nV_o}{Z_r}\sin[\omega_r(t - t_1)]. \tag{3}$$

4) *Mode d (t_3–t_4):* At the moment of t_3, the S_6 turn-ON signal arrives and S_6 achieves ZVS-ON. At this time, the transformer primary switching tubes S_1, S_4, and S_6 are turned ON. The resonant network structure is B-phase in parallel with C-phase and then in series with A-phase. The resonant frequency is f_r. The secondary side of the transformer is the same as the previous mode.

5) *Mode e (t_4–t_5):* At moment t_4, the secondary i_{Q2} is commutated past the zero point. The secondary current flows positively through Q_2, and flows through Q_3 parasitic diode to short-circuit the transformer T_2, T_3 secondary winding. At this time, V_{in} charges the resonant network and i_{Lr1}, i_{Lr2} and i_{Lr3} increase rapidly. The resonant network structure is the same as the previous mode.

6) *Mode f (t_5–t_6):* At the moment of t_5, the switching tubes S_3, S_4 change the current. During the dead time, i_{Lr2} is negative and i_{Lr2} charges and discharges the S_3, S_4 parasitic capacitors. After charging and discharging, the two ends of S_4 are charged to V_{in} and i_{Lr2} flows through the S_3 parasitic diode to renew the current.

7) *Mode g (t_6–t_7):* At the moment of $t6$, the S_3 turn-ON signal arrives and S_3 achieves ZVS-ON. At this time, the primary switching tubes S_1, S_3, and S_6 are turned ON and the secondary state is consistent with mode e. The primary

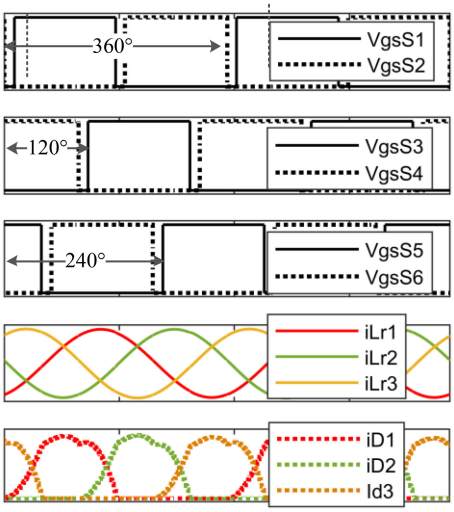

Fig. 4. Variable bus voltage mode: $f_s = f_r$.

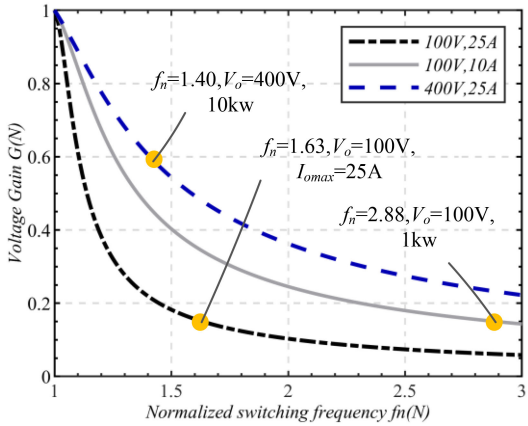

Fig. 5. Buck mode: voltage gain curve.

resonant network is AB-phase parallel and C-phase series. The primary resonant network is connected in parallel in phase AB and in series in phase C. V_{in} charges the resonant network and i_{Lr1}, i_{Lr2}, and i_{Lr3} increase rapidly.

8) *Mode h (t_7–t_8):* At the moment of t_7, Q_2 turns OFF, transformer T_2, T_3 is no longer short-circuited, and the secondary current flows through D_2 and Q_3 parasitic diodes for rectification. The resonant network is consistent with the previous mode, at this time, V_{in} and resonant network together discharge to the load.

B. Working Principle of Variable Bus Voltage Control and Buck Mode

The operating waveform of the SS-SA3PI resonant converter in variable bus voltage mode is shown in Fig. 4. The primary side switches S_1–S_6 operate in the same mode as Boost mode, and the secondary side Q_1–Q_3 switch signals are always low. S_1–S_6 realize ZVS-ON, D_1–D_3 and Q_1–Q_3 realize ZCS-OFF. In this mode, the input voltage is floating, $f_s = f_r$, the converter voltage gain is constant at 1, and the output voltage (660–850 V) is adjusted by adjusting the input voltage V_{in} (660–850 V). For example, when the desired output voltage is 750 V, we only need to adjust the input voltage to 750 V to achieve an output voltage of 750 V.

In buck mode, the bus voltage is fixed at 660 V. The converter primary side switching tubes are complementary, each phase bridge arm is lagged 120° in turn, and the secondary side drive signal is often low. When the output voltage is 100–660V, $f_s > f_r$, the switching frequency is adjusted to reduce the voltage gain of the converter. In this mode, the primary-side switches S_1–S_6 achieve ZVS-ON and the secondary-side switches do not achieve ZCS, but considering that the secondary-side switch tubes and diodes are of SiC structure, the secondary-side reverse recovery losses can be ignored. The operating mode in variable bus voltage and buck mode can be referred as the operating mode in boost mode, except that the secondary-side semiactive control is correspondingly absent.

III. Characterization and Control

A. Conditions for ZVS Implementation

Under multimode modulation, the implementation of the primary side switching ZVS needs to rely on the resonant current to fully charge and discharge the switching tube junction capacitance during the dead time, which needs to meet

$$L_{m\max} < \frac{t_{\text{dead}}}{16 C_{\text{oss}} f_s}. \tag{4}$$

In (4), t_{dead} is the dead time and C_{oss} is the ZVS equivalent charge/discharge capacitance. When the converter works in boost mode, the implementation of the transformer's secondary switching tubes Q_1 –Q_3 ZVS is the simplest, because the rectifier current does not flow through the switching tubes before the secondary switching tubes turn ON, and the switching tube DS voltage is always 0.

B. Voltage Gain

1) *Buck and Variable Bus Voltage Control Mode:* In these mode, the dc gain of the SS-SA3PI resonant converter is (5) [10]. In (5), n_p is the number of turns of the primary winding of the transformer, n_s is the number of turns of the secondary winding of the transformer. k is the inductance ratio, f_n is the normalized switching frequency, and Q is the quality factor of the converter. R_{ac} is the equivalent ac equivalent load to the primary side of the transformer. R is the output load equivalent resistance value.

Considering the limit working condition, the minimum output voltage at constant power in this mode is 400 V, the minimum output voltage at nonconstant power is 100 V, and the current limit is 25 A. From (5), Fig. 5 can be made. From Fig. 5, at $f_n = 1.4$, the full load $V_o = 400$ V; at $f_n = 1.63$, the maximum output current $I_{o\max} = 25$ A, $V_o = 100$ V; at $f_n = 2.88$, the light load,

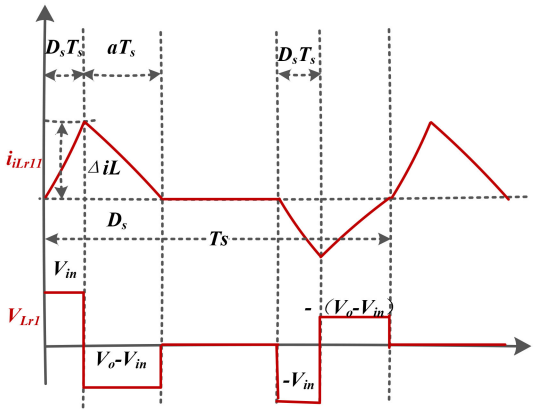

Fig. 6. i_{Lr11} and V_{Lr1} curve.

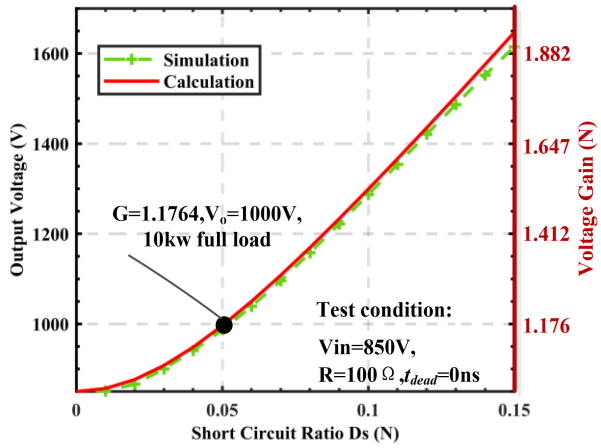

Fig. 7. Boost mode: Voltage gain curve.

$V_o = 100$ V, the voltage gain meets the requirement

$$M = \frac{V_{\text{out}}}{V_{\text{in}}} = \frac{1}{n}\frac{1}{\sqrt{\left(1+k-\frac{k}{f_n^2}\right)^2 + Q^2\left(f_n-\frac{1}{f_n}\right)^2}}$$

$$k = \frac{L_r}{L_m}, Q = \frac{\sqrt{L_r/C_r}}{n^2 R_{\text{ac}}}, n = \frac{n_p}{n_s}, f_n = \frac{f_s}{f_r},\ R_{\text{ac}} = \frac{6}{\pi^2}Rn^2. \tag{5}$$

2) *Boost Mode:* In this mode, the switching frequency $f_s = f_r$, then the converter ac gain is 1. According to the above modal analysis and waveform, it is known that the excitation current i_{Lm1} rises to i_{Lr1} at the moment t_4 and the secondary side current i_{Lr11} is intermittent as shown in Fig. 6. From the inductance voltage $V_{in} = L_r \times d_{iLr11}/d_t$ we know that

$$\Delta I_L = \frac{V_{\text{in}} D_s}{L_r f_s}. \tag{6}$$

According to the volt-sec balance relation of the inductor voltage under steady-state conditions, it is obtained that

$$V_{\text{in}} D_s T_s = (V_o - V_{\text{in}}) a T_s. \tag{7}$$

The diode current switching cycle average and load current are

$$I_D = \frac{1}{2}\Delta I_L a, I_o = \frac{V_o}{R}. \tag{8}$$

In steady state, the average value of diode current switching cycles is equal to the load current. Based on this, for i_{Lr1}, which is short-circuited twice per cycle, the output voltage gain M_{boost} can be expressed as

$$M_{\text{boost}}(f_s, L_r, D_s, R) = \frac{V_{\text{out}}}{V_{\text{in}}} = \frac{1}{2} + \sqrt{\frac{1}{4} + \frac{2D_s^2 R}{L_r f_s}}. \tag{9}$$

Equation (9) can be further expressed as

$$V_o = f(D_s) = \frac{V_{\text{in}} P L_r f_s}{P L_r f_s - 2D_s^2 V_{\text{in}}^2}. \tag{10}$$

When operating in boost mode, the converter has a constant maximum power output, then $V_{\text{in}}, P, L_r, f_s$ are constants in (10), and (9) is reduced to a univariate function $V_o = f(D_s)$, which is easy to implement in the online controller. Equations (9) and (10) are verified in MATLAB/Simulink to obtain Fig. 7, which shows that the theoretical calculation matches the simulated gain. Since the input voltage $V_{\text{in}} = 850$ V and the maximum output voltage $V_{o\max} = 1000$ V in Boost mode, the circuit requires the maximum gain $M_{\text{boostmax}} = 1.1764$. Considering the dead time of the converter, the gain loss caused by the rise/fall and turn-ON/OFF delay time of the switching tubes, the designed boost gain range is far more than 0.15 at $D_{s\max} = 0.15$. The designed boost gain range meets the requirements.

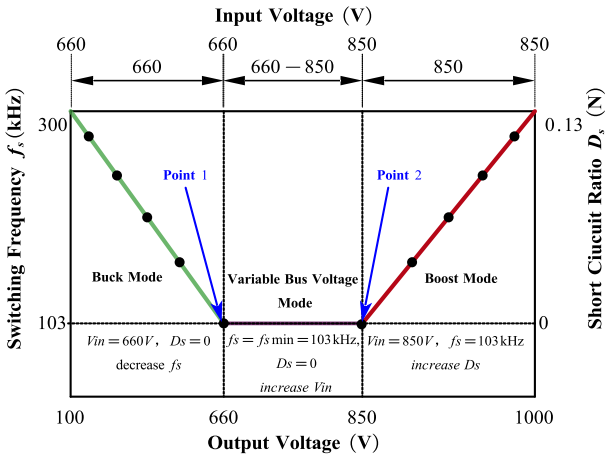

Fig. 8. Example of output voltage regulation.

C. Multimode Modulation

From the above analysis, we can see that the multimode modulation strategy uses three different control methods, and we name the three different control methods used as three modes. The selection of the mode is based on the output voltage as can be seen in Fig. 8. Also, Fig. 8 shows an example of the output voltage varying from 100 to 1000 V, with the transition and control variables changing for each mode:

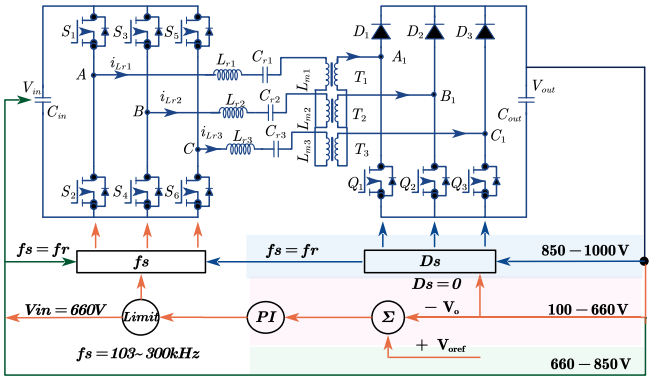

Fig. 9. Control block diagram.

At the output voltage range of 100–660 V, the input voltage V_{in} is fixed at 660 V, $D_s = 0$, the switching frequency f_s is gradually reduced to improve the voltage gain, until f_s reaches $f_{s\min}$, $f_s = f_r$, $V_{\text{out}} = 660$ V. At this time the voltage gain is 1, $V_{\text{out}} = V_{\text{in}}$. When the output voltage needs to continue to increase, the converter enters the next mode.

At the output voltage range of 660–850V, $f_s = f_r$, $D_s = 0$, the voltage gain is fixed to 1. When the output voltage needs to continue to increase from 660 V, the converter only needs to gradually increase the input voltage V_{in} to achieve the output voltage regulation. Until the output voltage reaches 850 V, the switching frequency and input voltage regulation will no longer increase the gain of the converter, then the converter enters the next mode.

At the output voltage range of 850–1000 V, $f_s = f_r$, $V_{\text{in}} =$ 850 V. When the output voltage needs to continue to increase from 850 V, the converter only needs to gradually increase D_s to achieve the output voltage regulation. When D_s increases to 0.13, the converter reaches its maximum voltage gain point and achieves an output of 1000 V.

From this example we can see that the converter goes through three modes when the output voltage changes from 100 to 1000 V. Among them, the converter mainly involves two mode transition points: Points 1 and 2. They correspond to output voltages of 660 and 850 V, respectively. According to the above voltage gain analysis, the voltage gain of the two transition points points 1 and 2 is 1. In addition, the converter has a constant 10 kW output when the output voltage is 400 V or more. Therefore, the mode transition of the converter does not involve a change in voltage gain or power. Thus, the problem of dynamic transition stability is eliminated.

The control block diagram of this article is given in Fig. 9. When the desired output voltage is lower than 660 V, the MCU of the converter fixes the bus voltage of the PFC to 660 V through SCI communication, and then controls the D_s to 0 to reduce the voltage gain. Finally, the switching frequency is adjusted to achieve the desired output voltage. When the desired output voltage range is between 660–850 V, the PI regulator output f_s is saturated. At this point, adjust V_{in} to obtain the desired output voltage. When the desired output voltage is higher than 850 V, both the controlled quantity input voltage V_{in} and the switching frequency f_s are saturated. At this time, increase D_s to increase the voltage gain of the converter to achieve the desired output voltage.

IV. Design Considerations

A. Selection of the Frequency

Core losses account for a large component of the losses in high power isolation converters. We choose Mn-Zn ferrite made of PC95 as the core of the magnetic element. This material has a large reduction in core loss in the range of 25° to 100° compared to PC40 material. Combining the loss of the magnetic core datasheet and considering the converter heat dissipation mode, power density, control mode and stability, the resonant frequency and the maximum switching frequency in the constant power range are designated as 100 and 140 kHz. Also, in the nonconstant power voltage range ($V_{\text{outmin}} = 100$ V), the maximum switching frequency is designed to be three times the resonant frequency, i.e., 300 kHz, to obtain a large voltage step-down effect.

B. Resonant Parameter Design

According to (4), we only need to determine t_{dead} and C_{oss} to obtain the $L_{m\max}$ value. Considering the turn-ON/ OFF delay time of the SiC switch and the safety margin, the t_{dead} was determined to be 200 ns. In order to reduce the *dv*/*dt* of the switching tubes and the midpoint of the bridge arm of each phase, so as to achieve the reduction of switching turn-OFF losses and improve EMI, we generally in parallel with an additional capacitor $C_{\text{DS}} = 1$ nF between the switching tubes DS. And C_{oss} in (4) should be $C_{\text{DS}} + C_{\text{ossmos}}$. Considering the nonlinearity of the switching tube C_{ossmos} and the ZVS margin we design the L_m value as 50% of $L_{m\max}$, so $L_m = 50$ uH.

As mentioned before, based on loss considerations, we set the maximum switching frequency of the converter at 140 kHz for the constant power case, which is 660 V input and 400 V 10 kW output. According to (2) and (5), we decouple the formula of Q. The decoupled Q can be expressed as

$$Q = \frac{2\pi f_r L_r}{n^2 R_{\text{ac}}}. \tag{11}$$

The parameter solutions of L_r can be calculated by (11) and (5) when f_n, f_r, L_m, and R_{ac} are known. C_r can be calculated according to (2).

C. Resonant Component Design

The design of magnetic components is concerned with only two things: whether the core will saturate (considering losses at high frequencies) and whether the windings will overheat. And the core evaluation equation for transformers and inductors can be expressed as

$$B_{Lr\max} = \frac{i_{Lr\max} L_r}{A_e N_{Lr}}, B_{T\max} = \frac{E_{T\max}}{4 f_s A_e N_p} \tag{12}$$

where $i_{Lr\max}$ can be calculated according to (1), and the maximum value of the average voltage on the transformer is

$$E_{T\max} = \frac{2}{T}\left(\int_0^{t_2} V_{AN}dt + \int_{t_2}^{t_4} V_{AN}^2 dt + \int_{t_4}^{t_8} V_{AN}^2 dt\right) = \frac{4}{9}V_{in\max}. \quad (13)$$

D. Discussion of Voltage and Current Stress

Once the resonance parameters are determined, we can discuss the voltage and current stresses on the switching tubes of the converter. In the soft switching converter, the voltage stress of the primary side switch tube is $V_{\text{inmax}} = 850$ V, and the voltage stress of the secondary side switch tube is $V_{\text{outmax}} = 1000$ V. Considering the resonance caused by the distribution parameters during the turn-ON and turn-OFF of the converter, the withstand voltage of the switching tubes should have a margin of 20%.

According to the operating principle of the converter, we know that when the input voltage is 660 V and the output voltage is 400 V, the current stress of the converter is maximum. The RMS value of the current on the primary side of the converter can be expressed as

$$i_{\text{pri\_rms}} = \frac{\pi}{3\sqrt{2}} \times \frac{P_{\text{outmax}} N_s}{V_{\text{out}} \eta N_p} \quad (14)$$

where η is the efficiency of the converter, we take 0.95 in the calculation of stress. The excitation current of the transformer can be expressed as

$$i_{Lm\_\text{rms}} = \frac{E_{T\text{rms}}}{2\pi f_r L_m} \quad (15)$$

where the transformer voltage RMS value $E_{T\text{rms}}$ is

$$E_{T\text{rms}} = \sqrt{\left(\frac{V_{in}}{3}\right)^2 \times \frac{2}{3} + \left(\frac{2V_{\text{in}}}{3}\right)^2 \times \frac{1}{3}}. \quad (16)$$

According to (13)–(15), we can know that the primary side current stress is also the peak resonant current is

$$i_{Lr\_\max} = \sqrt{2} \times \sqrt{(i_{Lm\_\text{rms}})^2 + (i_{\text{pri\_max}})^2}. \quad (17)$$

The current stress on the secondary side is the same as the primary side because the ratio of the transformer is 1.

E. Parameter Design Process

The parameter design process is shown in Fig. 10. The hardware parameters can be initially determined according to the parametric design flow, and then the design flow can be gradually adjusted according to the loss analysis and hardware layout.

V. Experimental Verification and Discussion

To evaluate the performance of the SS-SA3PI resonant converter, an experimental prototype was built. The pictures and parameters of the prototype are shown in Fig. 11 and Table I. The experimental prototype has a size of 250∗210∗36.6 mm and achieves a power density of 5.2 kW/L. The cooling of the experimental prototype is forced air cooling, provided by two fans.

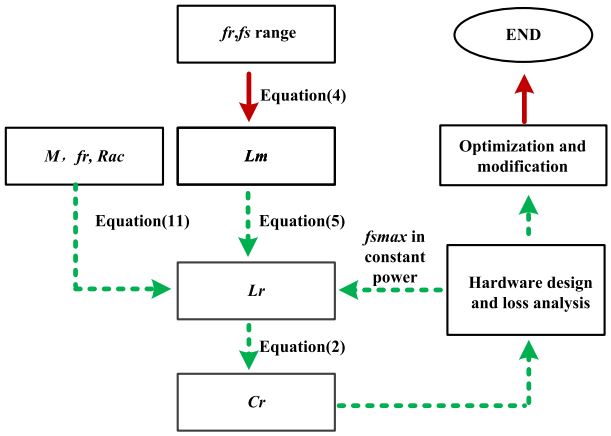

Fig. 10. Parameter design process.

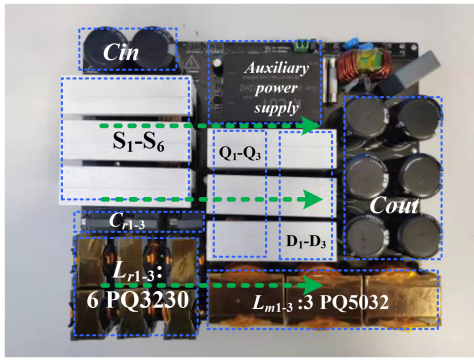

Fig. 11. Experimental prototype.

TABLE I
Detailed Parameters of the Hardware

Symbol	Detail	Symbol	Detail
f_r	103 kHz	S_1–S_6	UF3C120040K4S
f_s	103–300 kHz	Q_1–Q_3	UF3C120040K4S
L_r	24 uH	D_1–D_3	FFSH40120ADN
C_r	99 nF	V_{in}	660–850V
L_m	50 uH	V_{out}	100–1000V
n_p:n_s	10:10	I_{omax}	25 A
C_{out}	270 uF	P_{omax}	10 kW
L*W*H:250*210*36.6mm		Power dentist：5.2 kW/L	
Constant maximum power at output voltage 400–1000 V			

The green arrow in Fig. 11 represents the fan wind direction, and the prototype leaves a slight gap in each component to improve heat dissipation.

A. Experimental Performance

Fig. 12 shows the waveform for 400 V 25 A in buck mode with an input voltage of 660 V. From Fig. 12, we can see that $i_{Lr1}>0$ when S_2 is turned ON, the resonant current flows through the S_2 parasitic diode let S_2 achieves ZVS-ON, and similarly, S_1–S_6 are also ZVS-ON. Besides, when S_1 turn-OFF, V_{dsS1} and V_{gsS1}

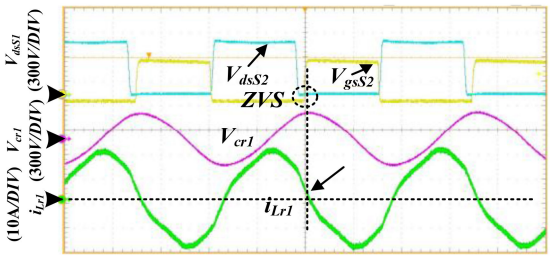

Fig. 12. ZVS realization waveform: $V_{\text{in}} = 660$ V, $V_{\text{out}} = 400$ V $I_{\text{out}} = 25$ A; and $f_s = 143$ kHz at 10 kW.

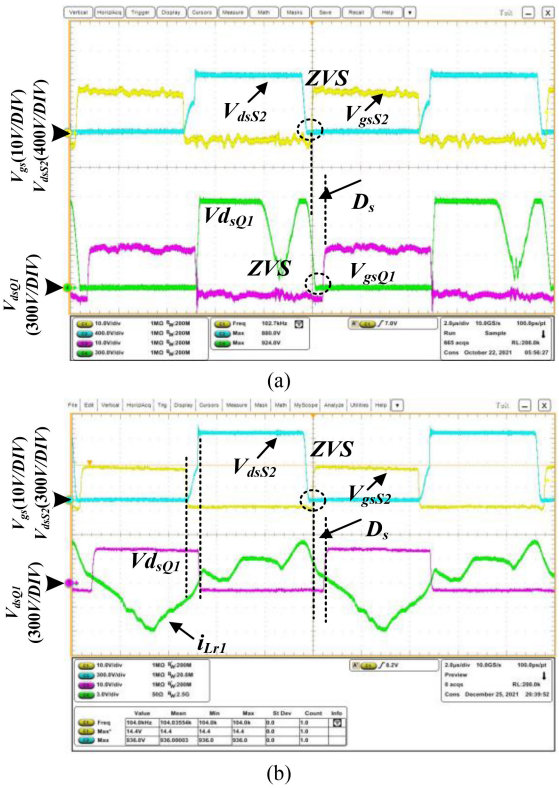

Fig. 13. Boost mode: secondary-side semiactive control. (a) $f_s = f_r$, $V_{\text{in}} =$ 800 V, $V_{\text{out}} = 924$V, 8.5kW, $D_s = 0.07$, and $G = 1.155$. (b) $f_s = f_r$, $V_{\text{in}} =$ 847V, $V_{\text{out}} = 977$V, 9.6kW, $D_s = 0.07$, and $G = 1.155$.

crossover is small, so the subsequent loss analysis ignores the turn-OFF loss.

Fig. 13 shows the waveform of the SS-SA3PI resonant converter in boost mode under secondary-side semiactive control in heavy load with $f_s = f_r$. From Fig. 13(a), it can be seen that the specific implementation of the semiactive boost control on the secondary side is achieved by adjusting the hysteresis phase shift angle of $Q_{1,\ 2,\ 3}$ with respect to $S_{2,\ 4,\ 6}$. Under this control, $G > 1$, the converter achieves boost operation. At the same time, ZVS-ON is achieved for both the primary and secondary side switching tubes. Fig. 13(b) shows the waveforms of V_{dsS2}, V_{gsS2},$V_{gsQ1,}$ and i_{Lr1} for a full-load input voltage of 850 V. Based on this, we can analyze that the resonant current i_{Lr1} is short-circuited in the secondary side winding of transformer T_1T_2 after S_2 is turned OFF and S_1 is turned ON, and i_{Lr1} rises

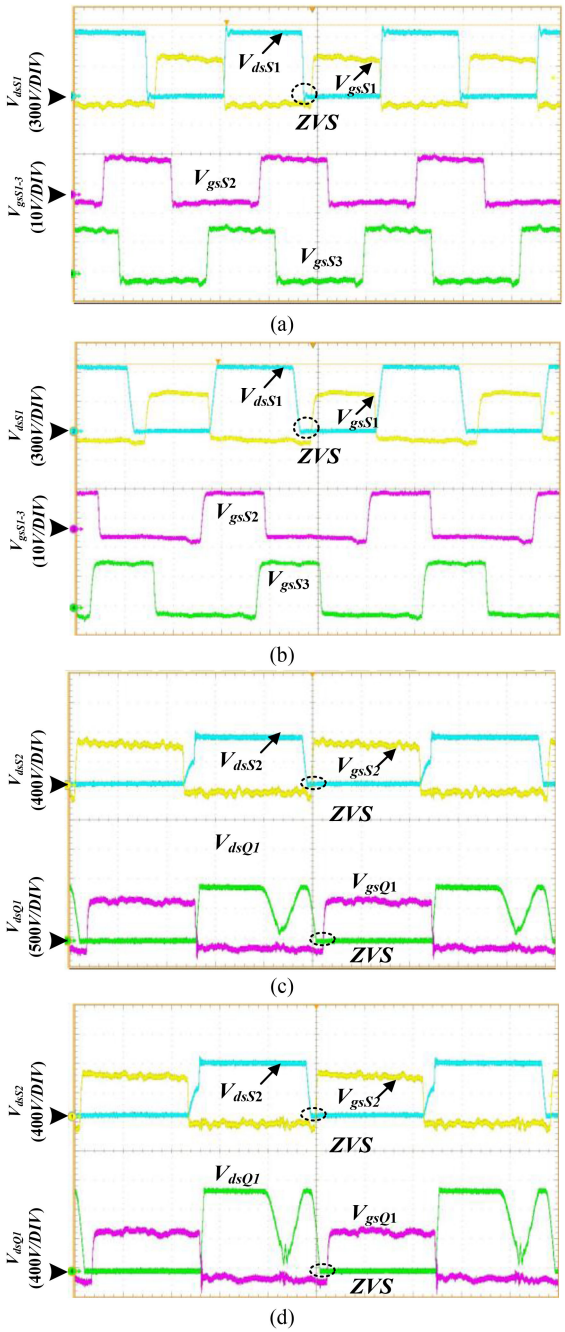

Fig. 14. ZVS implementation waveform. (a) $f_s = 155$ kHz, $V_{\text{in}} = 660$V, V_{out} $= 100$ V, 2.5 kW. (b) $f_s = 290$ kHz, $V_{\text{in}} = 660$ V, $V_{\text{out}} = 100$ V, 1 kW. (c) $f_s = f_r$, $V_{\text{in}} = 850$ V, $V_{\text{out}} = 900$ V, 1 kW. (d) $f_s = f_r$, $V_{\text{in}} = 850$ V, $V_{\text{out}} = 1000$ V, 1 kW.

rapidly and linearly, proving the charging process of the input voltage to the resonant network, thus, the boost operation of the converter is realized.

Fig. 14 shows the ZVS implementation waveform for the converter at different output voltages, especially at light loads. Fig. 14(a) shows the waveform diagram for a switching frequency of 155 kHz with an input voltage of 660 V and an output of 100 V 25 A. We can see that S_1 achieves ZVS-ON, and S_1, S_2, and S_3 drive signals are each lagged by 120°, it can

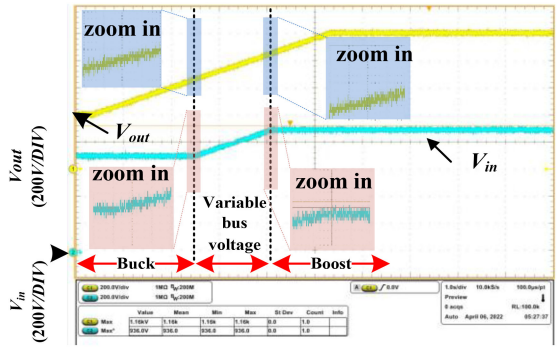

Fig. 15. Mode transition: output voltage is from 411V to 1003V.

be inferred that $S_{1\text{-}6}$ all achieve ZVS-ON, the converter works well. The most difficult situation for the converter to achieve ZVS is when the converter output voltage and output power are at their lowest, which is shown in Fig. 14(b). The switching frequency is 290 kHz with an input voltage of 660 V and an output of 100 V 10 A. We can see that the converter realizes ZVS. Also, Fig. 14(c) and (d) show the ZVS cases when the converter output conditions are 900 V 1 kW and 1000 V 1 kW. From all this, we can infer that the converter realizes ZVS soft switching under all working conditions.

The mode transition waveforms are shown in Fig. 15. From the figure, we can see that the converter experiences three modes when the output voltage changes from 411 to 1003 V. Moreover, there is no obvious overshoot of the output voltage at the two mode transition points. The converter employs the multimode modulation scheme achieves smooth mode conversion.

B. Measured Efficiency

Fig. 16(a) shows the efficiency curve of the converter for 100–1000 V. The maximum efficiency of the converter is 97.8925%, which is measured by the power analyzer LMG500, as shown in Fig. 16(b). And the loss distribution and calculation at this measurement efficiency is shown in Fig. 16(c), where the iron loss of the magnetic element is calculated by numerical fitting method. The rectification losses of diodes and switching tubes are mainly considered as ON-state voltage drop losses (V_D and V_Q are the average values at the highest and lowest temperatures), and S_1–S_6 are mainly considered as conduction losses (R_{on} is the average value at the highest and lowest temperatures). Since the parameters of the switching tubes and diodes vary greatly with temperature and device consistency, there is a 7.7 W difference between the loss calculation and the actual loss. Through the loss distribution chart we can see that the loss of the transformer at the highest efficiency is the main loss, which is because at this time the transformer $B_{\max}$ is 0.23 and the iron loss is higher. Also, this explains why the converter has the highest efficiency at 700 V output, because when the output voltage is higher, the transformer has a higher iron loss.

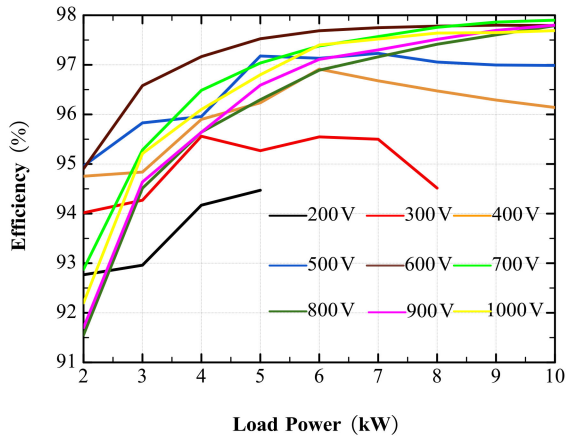

(a)

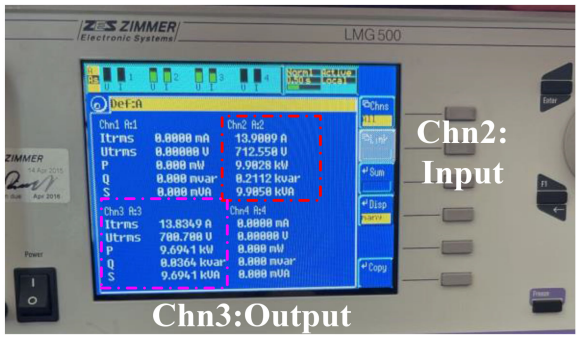

(b)

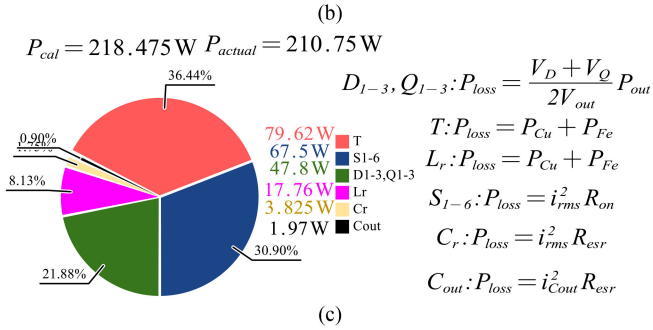

(c)

Fig. 16. Efficiency of SS-SA3PI resonant converter. (a) Efficiency under various working conditions. (b) Maximum efficiency. (c) Loss distribution at maximum efficiency.

C. Comprehensive Comparison With Similar Structures

We have made a comprehensive comparison of some similar structures. Among them, the structure of reference [33] is a three-level interleaved *LLC*. The common denominator of the compared structures is the presence of three symmetrical sets of resonant elements. However, the sizes and power density of the experimental prototypes are not described in detail. Some detailed comparison information is given in Table II and Fig. 17. In this case, the maximum voltage conversion ratio in Fig. 17(b) ignores the transformer ratio and compares only the voltage conversion ratio provided by the control method and the converter structure. It can be seen that the SS-SA3PI resonant converter using multimode modulation proposed in this article has obvious advantages.

TABLE II
COMPARISON WITH SIMILAR STRUCTURES

	This article	[3]	[4]	[21]	[33]
Structure	SS-SA3PI	Three-phase LLC	Three-phase interleaved LLC	Three-phase interleaved LLC	Three-level Three-phase interleaved SRC
Rated power	10 kW	5 kW	10 kW	3 kW	2 kW
Input voltage	660–850 V	600 V	360–400 V	400 V	440–590 V
Output voltage	100–1000 V	600 V	300 V	32–100 V	54–400 V
Max efficiency	97.89%	97.6%	97.88%	96%	96.5%
Additional components	No	No	No	Yes	No
Switching tubes	9 Mosfet+3 Diode	6 Mosfet+6 Diode	12 Mosfet+6 Diode	6 Mosfet+8 Diode	6 Mosfet+8 Diode
Power density	High	Low	Medium	Not given	Not given

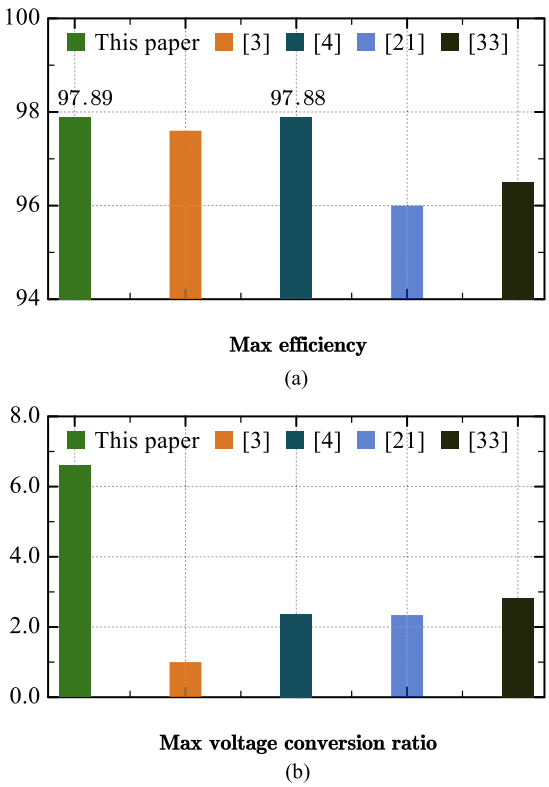

Fig. 17. Comparison. (a) Max efficiency. (b) Max voltage conversion ratio.

For a fuller comparison, we have compared our experimental prototypes with industrial products in detail. The comparison results are shown in Table III. It should be noted that the ac/dc and dc/dc converters are included in the off-board EV charger product. The overall structure of the product is that the ac/dc and dc/dc converter are mounted in a top and bottom pair. The length and width of the two converters are the same (420∗213 mm), but because the number of components in the ac/dc converter is small, it allows the components of the dc/dc converter to protrude(transformer). The volume of this part of the protruding element was also added to Table III to calculate the detailed

TABLE III
COMPARISON WITH INDUSTRIAL PRODUCT

	This article	[8]
Structure	SS-SA3PI	Three-level, three-phase interleaved LLC with ISOP/S
Rated power	10 kW	20 kW
Input voltage	660–850 V	660–850 V
Output voltage	100–1000 V	250–1000 V
Max efficiency	97.89%	98.1%
Size L*W*H	250*210*36.6 mm	420*213*40 mm + 108*73*33 mm
Power density	5.2 kW/L	5.2 kW/L
Additional components	No	Yes
Switching tube number	9 Mosfet+3 Diode	12 Mosfet+12 Diode

power density. From the comparison results in Table III, we can see that the output voltage range of this article is wider for the same input voltage and no additional components are added. However, one of the drawbacks of this article is that it has the same power density as the industrial product, but with slightly lower efficiency. This is mainly due to the following reasons.

1) The height of the transformer has been reduced for the sake of uniformity in the height of all components. This makes the transformer window area smaller and the number of turns ON the primary side smaller, resulting in a larger transformer B-value and reduced conversion efficiency.
2) The experimental prototype in this article contains the auxiliary power supply, while the auxiliary power supply for dc/dc of industrial products is located in the ac/dc converter.
3) The number of custom components also creates a disadvantage.

VI. Conclusion

The proposed SS-SA3PI resonant converter employing a multimode modulation scheme is well suited for high-power EV charger applications. This modulation scheme can greatly widen the output voltage regulation range of the converter without adding additional circuit components. It also avoids the problem of dynamic stability during mode transition. The use of secondary-side semiactive control in boost mode also reduces the design difficulty of resonance parameters and magnetic components. This all help to reduce the hardware cost and improve the power density of the converter. Moreover, the converter realizes soft switching under all working conditions and obtains high conversion efficiency. The experimental results show that the converter achieves an output voltage of 100–1000 V with a maximum conversion efficiency of 97.89% at a power level of 10 kW.

References

[1] L. Shuguang, Y. Zhenxing, and C. Gang, "Design and realization of high power density EV charging module," in *Proc. Chin. Control Decis. Conf.*, 2019, pp. 4909–4913.

[2] Z. Li, X. Yang, and Y. Li, "Design and implementation of a High-efficiency DC/DC converter for EVs charging basing on LLC resonant topology and silicon-carbide devices," in *Proc. IEEE Int. Power Electron. Appl. Conf. Expo.*, 2018, pp. 1–6.

[3] Y. Nakakohara, H. Otake, and T. M. Evans, "Three-Phase LLC series resonant DC/DC converter using SiC MOSFETs to realize high-voltage and high-frequency operation," *IEEE Trans. Ind. Electron.*, vol. 63, no. 4, pp. 2103–2110, Apr. 2016.

[4] H. Kim, J. Baek, and M. Ryu, "The high-efficiency isolated AC–DC converter using the three-phase interleaved LLC resonant converter employing the Y-Connected rectifier," *IEEE Trans. Power Electron.*, vol. 29, no. 8, pp. 4017–4028, Aug. 2014.

[5] Z. Shi, Y. Tang, and Y. Guo, "Optimal design method of LLC Half-bridge resonant converter considering backflow power analysis," *IEEE Trans. Ind. Electron.*, vol. 69, no. 4, pp. 3599–3608, Apr. 2022.

[6] Z. Li, B. Xue, and H. Wang, "An interleaved secondary-side modulated LLC resonant converter for wide output range applications," *IEEE Trans. Ind. Electron.*, vol. 67, no. 2, pp. 1124–1135, Feb. 2020.

[7] H. Vu and W. Choi, "A novel dual full-bridge LLC resonant converter for CC and CV charges of batteries for electric vehicles," *IEEE Trans. Ind. Electron.*, vol. 65, no. 3, pp. 2212–2225, Mar. 2018.

[8] Shijiazhuang Tonghe Electronic Technology Co., Ltd. TH20F10025C7, Shijiazhuang, China. Aug. 2021. [Online]. Available: https://v4.cecdn.yun300.cn/100001_2102265146/%E6%96%B0%E8%83%BD%E6%BA%90%E4%BA%A7%E5%93%81%E6%89%8B%E5%86%8C.pdf

[9] Huawei Digital Power Technologies Co., Ltd. R100020G1, Shenzhen, China. Nov. 2021. [Online]. Available: https://support.huawei.com/enterprise/en/doc/EDOC1100147885/ed343e5d

[10] Shenzhen UU Green Power Electric Co., Ltd. UR75028-E, Shenzhen, China, Mar. 2022. [Online]. Available: http://www.uugreenpower.com/ur75028cpxq

[11] Shenzhen Megmit Electric Co., Ltd. MR750-60T, Shenzhen, China, Oct. 2019. [Online]. Available: https://www.megmeet.com/uploads/ued./file/20200220/6371781453561034573401754.pdf

[12] Shenzhen Sinexcel Electric Co., Ltd. SER 1000V SERIES, Shenzhen, China, Dec. 2020. [Online]. Available: https://en.sinexcel.com/evcharger/ser/SER%2020kW%20Power%20Module%20Brochure.pdf

[13] Shijiazhuang Tonghe Electronic Technology Co., Ltd. TH750Q61ND-AXX, Shijiazhuang, China. Aug. 2021. [Online]. Available: https://v4.cecdn.yun300.cn/100001_2102265146/%E6%96%B0%E8%83%BD%E6%BA%90%E4%BA%A7%E5%93%81%E6%89%8B%E5%86%8C.pdf

[14] Y. Wei, Q. Luo, and A. Mantooth, "Overview of modulation strategies for LLC resonant converter," *IEEE Trans. Power Electron.*, vol. 35, no. 10, pp. 10423–10443, Oct. 2020.

[15] L. Junkai, Y. Ge, and M. Liu, "Research on a new control strategy for reducing hard-switching work range of the three-phase interleaved LLC resonant converter," in *Proc. IEEE Int. Telecommun. Energy Conf.*, 2018, pp. 1–6.

[16] Y. Jang, M. M. Jovanović, and J. M. Ruiz, "Implementation of 3.3-kW GAN-based DC-DC converter for EV on-board charger with series-resonant converter that employs combination of variable-frequency and delay-time control," in *Proc. IEEE Appl. Power Electron. Conf. Expo.*, 2016, pp. 1292–1299.

[17] X. Sun, X. Li, Y. Shen, B. Wang, and X. Guo, "Dual-Bridge LLC resonant converter with fixed-frequency PWM control for wide input applications," *IEEE Trans. Power Electron.*, vol. 32, no. 1, pp. 69–80, Jan. 2017.

[18] W. Liu, B. Wang, W. Yao, Z. Lu, and X. Xu, "Steady-state analysis of the phase shift modulated LLC resonant converter," in *Proc. IEEE Energy Convers. Congr. Expo.*, 2016, pp. 1–5.

[19] S. Zong, H. Luo, W. Li, Y. Deng, and X. He, "Asymmetrical duty cycle-controlled LLC resonant converter with equivalent switching frequency doubler," *IEEE Trans. Power Electron.*, vol. 31, no. 7, pp. 4963–4973, Jul. 2016.

[20] L. Shih, Y. Liu, and Y. Luo, "Adaptive DC-link voltage control of LLC resonant converter," *CPSS Trans. Power Electron. Appl.*, vol. 3, no. 3, pp. 187–196, Sep. 2018.

[21] S. A. Arshadi, M. Ordonez, and W. Eberle, "Three-Phase LLC battery charger: Wide regulation and improved light-load operation," *IEEE Trans. Power Electron.*, vol. 36, no. 2, pp. 1519–1531, Feb. 2021.

[22] H. Li, Z. Zhang, S. Wang, J. Tang, X. Ren, and Q. Chen, "A 300-kHz 6.6-kW SiC bidirectional LLC onboard charger," *IEEE Trans. Ind. Electron.*, vol. 67, no. 2, pp. 1435–1445, Feb. 2020.

[23] Y. Wei, Q. Luo, X. Du, N. Altin, A. Nasiri, and J. M. Alonso, "A dual half-bridge LLC resonant converter with magnetic control for battery charger application," *IEEE Trans. Power Electron.*, vol. 35, no. 2, pp. 2196–2207, Feb. 2020.

[24] K. Harada, A. Katsuki, M. Fujiwara, H. Nakajima, and H. Matsushita, "Resonant converter controlled by variable capacitance devices," *IEEE Trans. Power Electron.*, vol. 8, no. 4, pp. 404–410, Oct. 1993.

[25] Z. Hu, Y. Qiu, L. Wang, and Y. Liu, "An interleaved LLC resonant converter operating at constant switching frequency," *IEEE Trans. Power Electron.*, vol. 29, no. 6, pp. 2931–2943, Jun. 2014.

[26] Y. Hu, A. Amara, and A. Ioinovici, "LLC resonant converter operated at constant switching frequency and controlled by means of a switched-capacitor circuit," in *Proc. 1st Int. Future Energy Electron. Conf.*, 2013, pp. 691–696.

[27] G. Liu, Y. Jang, and M. M. Jovanović, "Implementation of a 3.3-kW DC–DC converter for EV on-board charger employing the series-resonant converter with reduced-frequency-range control," *IEEE Trans. Power Electron.*, vol. 32, no. 6, pp. 4168–4184, Jun. 2017.

[28] Y. Jang, M. M. Jovanović, and J. M. Ruiz, "Series-resonant converter with reduced-frequency-range control," in *Proc. IEEE Appl. Power Electron. Conf. Expo.*, 2015, pp. 1453–1460.

[29] Z. Li and H. Wang, "Comparative analysis of high step-down ratio isolated DC/DC topologies in PEV applications," in *Proc. IEEE Appl. Power Electron. Conf. Expo.*, 2016, pp. 1329–1335.

[30] Y. Jang, M. M. Jovanović, and M. Kumar, "Isolated, bi-directional DC-DC converter for fuel cell electric vehicle applications," in *Proc. IEEE Appl. Power Electron. Conf. Expo.*, 2019, pp. 1674–1681.

[31] J. Kim and G. Moon, "A new LLC series resonant converter with a narrow switching frequency variation and reduced conduction losses," *IEEE Trans. Power Electron.*, vol. 29, no. 8, pp. 4278–4287, Aug. 2014.

[32] H. Wu, T. Mu, and X. Gao, "A secondary-side phase-shift-controlled LLC resonant converter with reduced conduction loss at normal operation for hold-up time compensation application," *IEEE Trans. Power Electron.*, vol. 30, no. 10, pp. 5352–5357, Oct. 2015.

[33] F. Liu, Y. Chen, and X. Chen, "Comprehensive analysis of three-phase three-level LC-Type resonant DC/DC converter with variable frequency control—Series resonant converter," *IEEE Trans. Power Electron.*, vol. 32, no. 7, pp. 5122–5131, Jul. 2017.

Zhe Shi was born in Hebei, China, in 1994. He received the B.S. degree in electrical engineering from the Department of Electrical Engineering, North Minzu University, Yinchuan, China, in 2017, and the M.S. degree in electrical engineering in 2020 from the Department of Electrical Engineering, Hebei University of Science and Technology, Tianjin, China, where he is currently working toward the Ph.D.degree in power electronics.

His current research interests include resonant converter, ultra-fast EV charger, and renewable power conversion system.

Yu Tang (Senior Member, IEEE), received the B.S. and Ph.D. degrees in electrical engineering from the Department of Electrical Engineering, Nanjing University of Aeronautics and Astronautics (NUAA), Nanjing, China, in 2003 and 2008, respectively.

Since 2008, he has been with the Department of Electrical Engineering, NUAA State Key Laboratory of State Key Laboratory of Reliability and Intelligence of Electrical Equipment, Hebei University of Technology since 2018. He has authored or coauthored more than 80 papers in journals and conference proceedings. His research interests include power electronics in renewable energy generation.

Dr. Tang is the Guest Associate Editor for the IEEE TRANSACTION ON POWER ELECTRONICS.

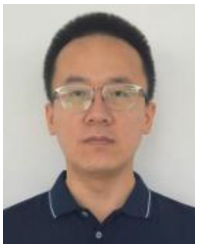

Yuliang Zhang received the B.S. degree in communication engineering from the Tianjin University, Tianjin, China, in 2008.

He is currently the Director and the Chief Engineer of Shijiazhuang Tonghe Electronic Technology Co., Ltd., Shijiazhuang, China. The company is a high-tech enterprise that has long focused on the R & D and manufacturing of power electronic power conversion equipment. His current research interests include resonant converter, ultrafast EV charger, and digital control of SMPS.

Yingjun Guo received the M.S. degree in electrical engineering from the Beijing Institute of Technology, Beijing, China, in 2004. He is currently working toward the Ph.D. degree in control theory and control engineering with the Hebei University of Technology, Tianjin, China. He is also an Associate Professor with the Hebei University of Science and Technology. His research interests include wind power control and power electronic devices.

Hexu Sun (Senior Member, IEEE) received the Ph.D. degree in automation from Northeastern University, Shenyang, China, in 1993.

He has been a Professor with the School of Control Science and Engineering, Hebei University of Technology, Tianjin, China, and the School of Electrical Engineering, Hebei University of Science and Technology, Shijiazhuang, China. He has authored five books and more than 130 journal and conference papers, and holds 13 U.S. patents and five computer software copyrights. His current research interests include robotics and complex engineering systems.

Dr. Sun is a recipient of many prestigious national awards from China. He was the Director of many societies and committees in China. He is currently the Invited Plenary Speaker and the General Co-Chair of many international conferences.

Lin Jiang (Member, IEEE), received the B.S. and M.S. degrees in electrical engineering from the Huazhong University of Science and Technology, Wuhan, China, in 1992 and 1996, respectively, and the Ph.D. degree in electrical engineering from the University of Liverpool, Liverpool, U.K., in 2001.

From 2001 to 2003, he was a Postdoctoral Research Assistant with the University of Liverpool, and from 2003 to 2005, he was a Postdoctoral Research Associate with the Department of Automatic Control and Systems Engineering, The University of Sheffield, Sheffield, U.K. From 2005 to 2007, he was a Senior Lecturer with the University of Glamorgam, Wales, U.K., and in 2007, he joined the University of Liverpool. He is currently a Reader with the University of Liverpool. His research interests include control and analysis of power system, smart grid, and renewable energy.